


Cite this: *Energy Adv.*, 2022,
1, 1065

High specific capacity and mechanism of a metal–organic framework based cathode for aqueous zinc-ion batteries†

Wenshan Gou,^a Hao Chen,^b Zhao Xu,^a Yifei Sun,^a Xuguang Han,^a Mengmeng Liu^a
and Yan Zhang  ^{*a}

Rechargeable aqueous zinc-ion batteries (AZIBs) are promising for large-scale energy storage due to their high safety and low cost but the reported cathode materials still suffer from limited specific capacities and poor cycle performance. Herein, the Mn-based metal–organic framework (MOF), MOF-73, is used for the first time to make a novel cathode for AZIBs and its great capacity enhancement mechanism is investigated. Results show that MOF-73 can render a voltage plateau of ~ 1.45 V and induce manganese ions to co-contribute a high-specific capacity of 815 mA h g^{-1} ($0.84 \text{ mA h cm}^{-2}$). This work sheds light on the fundamentals of the electrochemical zinc energy storage of MOFs while holding great promise for exploring novel MOFs as cathodes for AZIBs.

Received 21st September 2022,
Accepted 9th November 2022

DOI: 10.1039/d2ya00257d

rsc.li/energy-advances

1. Introduction

In recent decades, with the increasing prominence of energy issues and promoting carbon neutrality, the exploration and utilization of renewable energy resources have attracted tremendous attention across the world.¹ Lithium-ion batteries (LIBs) have been widely used as power sources in many fields. However, there has been much concern regarding the limited resources of lithium and safety issues.^{2–5} This has resulted in great interest in aqueous rechargeable zinc-ion batteries (AZIBs) because of the nonflammable nature of aqueous electrolytes and abundant zinc resources. Besides, AZIBs also possess the advantages of a facile manufacturing process and high ionic conductivity that is almost two orders of magnitude greater than those of non-aqueous electrolytes.^{6,7} Nevertheless, Zn^{2+} has a higher electric charge and higher molecular weight, which makes ions more difficult to insert/extract into/from electrode materials.⁸ Such problems seem to have become the bottlenecks for AZIBs practical applications in the energy storage field. At present, a considerable amount of literature has been focused on the improvement of the electrochemical performance of cathode materials, including Mn/V-based materials⁹ and Prussian blue analogs.¹⁰ Vanadium-based

cathode materials such as V_2O_5 ,¹¹ VO_2 ,¹² and VS_2 ¹³ have been widely studied due to their unique layered structure and excellent specific capacity and rate performance but most vanadium-based materials are toxic.¹⁴ Prussian blue analogs are also a large class of compounds that attract extensive attention due to their very stable frame structure that can realize the rapid insertion/extraction of zinc ions. However, they still suffer from the problem of low-storage capacity.¹⁵ Mn-based materials, such as MnO_2 ,^{16–19} Mn_2O_3 ,²⁰ and ZnMn_2O_4 ,²¹ have drawn much attention very recently but the problems of rapid capacity fading and poor rate performance limit their widespread use in AZIBs.²² Although the electrochemical performance can be boosted by material modification, there is still much room for further improvement. In addition to modifying the existing electrode materials, discovering new materials with excellent electrochemical properties, especially with high specificity, is also vital for the further development of AZIBs.²³

Different from conventional inorganic electrode materials, metal–organic frameworks (MOFs) as a unique class of porous crystalline materials has attracted much interest for many applications due to their huge variety of structures, large surface areas and adjustable porosity. These functional MOFs show great potential in many areas such as catalysis, drug delivery, gas separation and storage.²⁴ Examples of MOFs as electrode materials for lithium and sodium-ion batteries indicate that they have great potential in the energy storage field.^{25,26} The unique crystal structure and pore structure facilitate the diffusion of guest Li^+ and Na^+ .^{27,28} However, the investigation of MOFs as cathode materials for AZIBs is scarce and the attractive Zn^{2+} storage behaviors seem elusive. Thus,

^a Institute of Advanced Cross-field Science, College of Life Sciences, Qingdao University, Qingdao 200671, P. R. China. E-mail: yzhang_iacs@qdu.edu.cn^b School of Materials and Energy, Southwest University, Chongqing, 400715, P. R. China† Electronic supplementary information (ESI) available. See DOI: <https://doi.org/10.1039/d2ya00257d>

the exploration of new MOF-based cathode materials for AZIBs and the study of their zinc storage mechanism are essential for finding novel competitive AZIBs cathodes.²⁹

In this work, a manganese-based MOF (MOF-73) was explored as a novel cathode for AZIBs for the first time, and it delivers a high specific capacity of 815 mA h g⁻¹ (0.84 mA h cm⁻²) at 50 mA g⁻¹, along with a discharge voltage plateau range from 1.2 to 1.6 V. The great capacity enhancement mechanism was studied using various *ex situ* measurements. Results reveal that MOF-73 can facilitate the deposition of Zn₄SO₄(OH)₆ and Zn_xMnO(OH)_y, which co-contributes to the high specific capacity.

2. Experimental

2.1 Material synthesis

MOF-73 was synthesized according to a previous report.³⁰ Briefly, 1 mmol MnCl₂·4H₂O (Aladdin, analytically pure) and 3 mmol terephthalic acid (H₂TP Aladdin 99%) were dissolved in 30 mL of mixed solvent of 15 mL *N,N*-dimethylformamide (DMF Aladdin, analytically pure) and 15 mL ethanol. The white suspension was treated with ultrasound for 10 min, then vigorously stirred for 1 h, and transferred into a 50 mL Teflon-lined autoclave and heated at 180 °C for 24 h. The product was washed with DMF and alcohol several times, then dried at 60 °C overnight under vacuum.

2.2 Material characterization

X-ray diffraction (XRD) was carried out on an Ultra IV diffractometer (Japan Science Co., Tokyo, Japan) with Cu-Kα radiation ($\lambda = 0.15418$ nm) with the scan rate of 10° min⁻¹ over a 2-theta range from 5° to 55°. Scanning electron microscopy (SEM) analyses were conducted on a JEOL JSM-7800F microscope (Japan Electronics Co., Tokyo, Japan) to study the morphologies of the MOF-73. X-ray photoelectron spectroscopy (XPS) measurements were performed on a Thermo Scientific ESCA-Lab 250Xi⁺ (Thermo Fisher Scientific Co., Waltham, America) to investigate the chemical valence state. Fourier transform-infrared (FT-IR) spectroscopy was performed on a Frontier NIR Std spectrophotometer (Thermo Fisher Scientific Co., Waltham, America). The thermogravimetric analysis was conducted *via* differential scanning calorimetry (Netzsch Ltd STA409PC, DSC404F3) using Netzsch Instrumentation (Germany).

2.3 Electrochemical measurements

The CR2032-type coin cells (Guangdong Canrd New Energy Technology Co. Ltd, Guangdong, China) were assembled using Zn foil as the anode with a diameter of 12 mm (Guangdong Canrd New Energy Technology Co. Ltd, Guangdong, China), glass fiber as the separator (diameter-16 mm Whatman Co., Maidstone, England), and an aqueous solution of 2 M ZnSO₄ with 0.2 M MnSO₄ additives as electrolytes. The cathode was composed of active materials, acetylene black (AB) and polyvinylidene fluoride (PVDF Macklin, *M_w* = 1 000 000). They were

mixed in an agate mortar at the weight ratio of 7 : 2 : 1 with *N*-methyl-2-pyrrolidone (NMP) added. The working electrodes were prepared by spreading the obtained slurry onto the titanium foils and drying at 60 °C for 12 h in a vacuum oven. The mass loading of active materials in each electrode was about 1.2–1.8 mg. The cycle and rate performance were measured on a LAND battery test system CT3001A (Wuhan LAND Electronic Co. Ltd, Wuhan, China). The cyclic voltammetry (CV) measurements were carried out using a CHI760E electrochemical workstation (Shanghai Chenhua Instrument Co., Shanghai, China) at a scan rate of 0.3 mV s⁻¹.

3. Results and discussion

To identify the phase composition of the as-prepared samples, XRD measurements were performed. The collected patterns in Fig. 1a display sharp peaks and match well with the simulated patterns from the single crystal data [CCDC No. 265094 Mn₃(TP)₃(DMF)₂], indicating the excellent crystallization and purity of the as-synthesized MOF-73.³¹ Fig. 1b is a view of the crystalline framework of MOF-73, in which the Mn-carboxylate structure (Fig. 1b left) with a pair of 6-coordinated Mn(II) as the polyhedron forms the secondary building units (SBUs). Those SBUs are linked together (Fig. 1b right) *via* benzene units of 1,4-benzenedicarboxylic. The tape of Mn–O–C rods of this MOF is coordinated with modes as exhibited in Fig. S1 (ESI[†]). The morphology of the as-synthesized MOF-73 was investigated using scanning electron microscopy (SEM) as shown in Fig. 1c. The rod-like micro-particles are composed of small units stacked in layers. The EDS mapping (Fig. 1d) demonstrates that C, O and Mn elements are uniformly distributed.

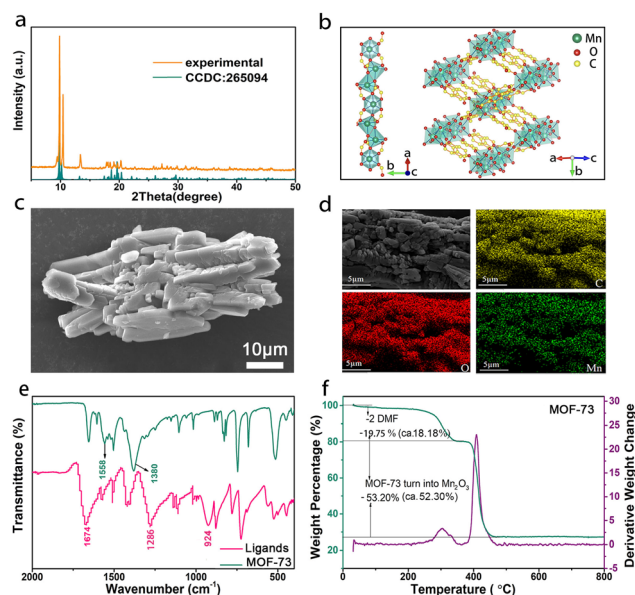


Fig. 1 (a) XRD pattern of as-synthesized MOF-73. (b) Crystal structure of MOF-73. (c) SEM images and (d) EDS mapping. (e) FTIR spectra and (f) TGA curve of the as-prepared MOF-73.



The FT-IR spectrum of the as-prepared MOF-73 in Fig. 1e shows a typical C=O stretching vibration at 1674 cm^{-1} , as well as the δOH^- and νCO coupling vibration of carboxylic acid ($-\text{COOH}$) groups at 1286 and 924 cm^{-1} . After coordination with Mn^{2+} , the C=O stretching vibration and δOH^- and νCO coupling vibration of carboxylate groups ($-\text{COO}^-$) vanished. Two bands appeared at 1558 and 1380 cm^{-1} , attributed to the asymmetric and symmetric stretching of carboxylic acid, indicating that the carboxyl hydrogen of H_2TP was completely replaced.³² The above change in the characteristic functional group proves that the coordination with Mn^{2+} occurs and results in the formation of MOF-73. Fig. 1f is the thermogravimetric analysis (TGA) curve from room temperature to 800°C in air. According to the chemical formula $[\text{Mn}_3(\text{TP})_3(\text{DMF})_2]$ of MOF-73, the mass loss (19.75%) from 250 to 350°C is due to the loss of DMF molecules, which agrees well with the value of 18.18% calculated according to its chemical formula. The XRD pattern after calcining at 800°C in the air is consistent with the standard Mn_2O_3 card (Fig. S2, ESI†), and thus the weight loss (53.20%, *ca.* 52.30%) in the range of 350 – 450°C is attributed to the thermal decomposition of MOF-73 to Mn_2O_3 . X-ray photoelectron spectra (XPS) of the as-prepared MOF-73 are displayed in Fig. S3 (ESI†). The $\text{Mn}2\text{p}$ core level spectrum (Fig. S3b, ESI†) displays doublets for $\text{Mn}2\text{p}_{3/2}$ and $\text{Mn}2\text{p}_{1/2}$ at 641.13 and 653.04 eV , respectively, and their main doublets are separated by $\sim 12\text{ eV}$, indicating that the Mn ions in MOF-73 are divalent. The binding energy of $\text{O}1\text{s}$ (Fig. S3c, ESI†) peaks can be assigned to oxygen in the hydroxyl ($\text{C}-\text{O}^-$) and carbonyl ($\text{C}=\text{O}$) groups, respectively.³³ The binding energies of the $\text{C}1\text{s}$ emission peaks in Fig. S3d (ESI†) fit quite well with one peak at 285.4 eV (H_2TP , phenyl carbons) and another peak at 288.53 eV (H_2TP , carboxyl carbons).^{30,34} Our results, therefore, demonstrate that the MOF-73 was successfully synthesized.

Electrochemical tests were performed with the as-prepared MOF-73 cathodes. As shown in Fig. 2a, two oxidation peaks ($\sim 1.75\text{ V}$, $\sim 1.80\text{ V}$) were observed in the first anodic scan of CV curves. The peak at $\sim 1.75\text{ V}$, different from the oxidation peaks in the second and third anodic scans, indicates a possible irreversible oxidation process in the first anodic scan. Another oxidation peak at $\sim 1.80\text{ V}$ corresponds to its reduction peak at $\sim 1.45\text{ V}$ and this pair of redox peaks remain in the following scans. Unlike other reported materials using the same electrolyte,^{35–37} this strong and stable couple of redox peaks are derived from the reversible insertion/extraction of Zn^{2+} into/from MOF-73. This is in sharp contrast to the steadily weakening peaks without added Mn^{2+} in (Fig. S4, ESI†). After the first cycle, two entirely new oxidation peaks emerged at 1.55 and 1.60 V . The redox peaks ($\sim 1.60/\sim 1.35\text{ V}$) could be attributed to the reversible redox of $\text{Mn}^{2+}/\text{Mn}^{4+}$ and another pair of peaks ($\sim 1.55/\sim 1.20\text{ V}$) is similar to the peaks in Fig. S4 (ESI†), which could be attributed to sedimentation/resolution of manganese and $\text{Zn}_4\text{SO}_4(\text{OH})_6\cdot 4\text{H}_2\text{O}$ on the electrode surface. It also could be observed that those new redox peaks have a mild increase in the following cycles, which is consistent with the rising specific capacity. The capacity-increasing phenomenon is common in Mn^{2+} -containing electrolyte systems. To exclude the influence

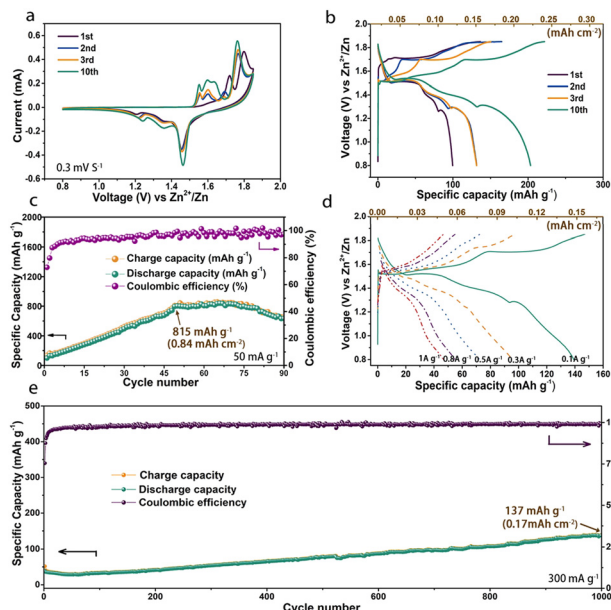


Fig. 2 (a) CV curves, (b) voltage profiles, (c) cycle performance, (d) rate performance and (e) long cycle performance of the MOF-73 cathode.

of the electrolyte on the high capacity, we also constructed this cell system using bare carbon material electrodes, as shown in Fig. S6 (ESI†). The bad electrochemical performance of this carbon material indicated that the capacity of the battery is not from the electrolyte. Particularly, MOF-73 not only possesses a higher capacity but its carboxyl groups also can promote the sedimentation of Mn^{2+} on the electrode surface.³⁷ In keeping with the CV curves, a discharge voltage plateau at about 1.45 V could be observed in the voltage profiles (Fig. 2b) and the specific capacity gradually increased to 815 mA h g^{-1} (0.84 mA h cm^{-2}) after 50 cycles and began to decrease starting at about the 75th cycle (Fig. 2c). Coinciding with some recent studies,³⁶ the mildly increased capacity in the first 50 cycles is associated with the deposition–dissolution of $\text{Zn}_4\text{SO}_4(\text{OH})_6\cdot 4\text{H}_2\text{O}$, which co-contributes to a high capacity in Mn^{2+} -containing AZIB systems. The rate performance is another key parameter that allows a fast charge rate in practice. As shown in Fig. 2d, the MOF-73 cathode exhibited discharge-specific capacities of 142.6 , 100.8 , 77.2 , 54.9 and 46.9 mA h g^{-1} (corresponding to 0.15 , 0.11 , 0.08 , 0.06 and 0.05 mA h cm^{-2}) at current densities of 0.1 , 0.3 , 0.5 , 0.8 and 1 A g^{-1} , respectively. The long-term cycle performance testing at 0.3 A g^{-1} is shown in Fig. 2e. Restricted by its relatively low intrinsic electronic conductivity, there is still some progress to be made in the rate performance of MOF-73. In this case, strategies such as doping with metal ions and compositing with highly conductive materials could be used for improved rate performance. After 1000 cycles, the specific capacity achieved 137 mA h g^{-1} . It is very interesting to observe that the capacity keeps increasing during the whole cycle tests. We argue that this result may hint that Zn ions inserted in MOF-73 require an activation process to continuously form electrochemically reversible species during the charge/discharge process. Longer cycle experiments associated



with the *in situ* monitoring of the charge/discharge process were designed to explore the deep fundamentals. Table S1 (ESI[†]) compares the electrochemical performances of many previously reported manganese-based materials used in AZIBs with that of our MOF-73-based material, clearly indicating that our device has prominent performance.

To analyze the Zn^{2+} storage mechanism of MOF-73, detailed characterizations were performed. The *ex situ* XRD patterns of the MOF-73 cathode at different states a (0.80 V), b (1.55 V), c (1.60 V), d (1.76 V), e (1.85 V), f (1.45 V), g (1.35 V), h (1.20 V) are shown in Fig. 3a. *Ex situ* XRD patterns demonstrate the reversible phase change of the electrode. The peaks in this charge–discharge cycle fit well with the standard card of $\text{Zn}_4\text{SO}_4(\text{OH})_6 \cdot 5\text{H}_2\text{O}$. It was observed that the intensities of those peaks vary with potential. In addition to the extraction of Zn^{2+} from MOF-73 in the charging process (from 0.80 V to 1.85 V), the partial deintercalation of Zn^{2+} and H^+ is accompanied by the dissolution of the $\text{Zn}_4\text{SO}_4(\text{OH})_6 \cdot 5\text{H}_2\text{O}$ characteristic peaks. In the discharge process (from 1.85 V to 0.80 V), characteristic peaks of deposited $\text{Zn}_4\text{SO}_4(\text{OH})_6 \cdot 5\text{H}_2\text{O}$ emerged again due to the intercalation of Zn^{2+} and H^+ .³⁸

To further investigate the reaction of Mn^{2+} species in the electrode, *ex situ* XPS was performed at different states of the charging process. The core-level spectra of O1s are displayed in Fig. 3b. These can be divided into two prominent peaks. The peak around 531.7 eV at states d and e is associated with the Mn–OH bond which belongs to the $\text{Zn}_x\text{MnO}(\text{OH})_y$. During the charging process, the $\text{Zn}_4\text{SO}_4(\text{OH})_6 \cdot 5\text{H}_2\text{O}$ can drive the Mn^{2+} in the electrolyte to undergo an electrodeposition reaction, thereby forming $\text{Zn}_x\text{MnO}(\text{OH})_2$ on the electrode. In the subsequent discharge process, the $\text{Zn}_x\text{MnO}(\text{OH})_2$ also undergoes a proton solid-phase reaction but its high activity and the reformation of $\text{Zn}_4\text{SO}_4(\text{OH})_6 \cdot 5\text{H}_2\text{O}$ can change the pH value of the electrode surface, causing the $\text{Zn}_x\text{MnO}(\text{OH})_2$ dissolution at the fully discharged state.²⁹ The XPS peaks of Mn–OH disappeared at the fully discharged state. Another peak at 529.7 eV is consistent with the typical Mn–O–Mn bond for tetravalent MnO_2 .³⁹ For scans of $\text{Mn}2\text{p}_{3/2}$ and $2\text{p}_{1/2}$, the peaks located at 642.3 eV and 653.9 eV (Fig. 3c) fit very well with the plain MnO_2 peak-pair pattern, evidencing the presence of Mn^{4+} .⁴⁰ The peak

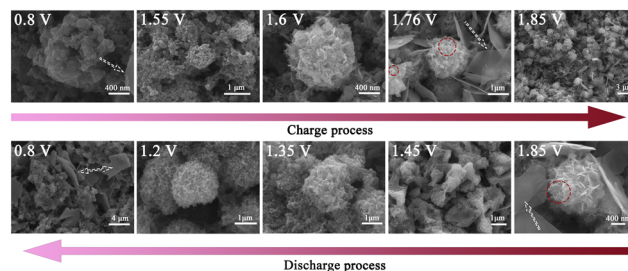


Fig. 4 The *ex situ* SEM images of the MOF-73 cathode at different states.

of MnO_2 ($\text{Mn}2\text{p}_{3/2}$, $2\text{p}_{1/2}$) also exists in the full-discharge state, and we deduce that some irreversible MnO_2 is formed in the previous cycles.

The surface morphology evolution of the MOF-73 electrode during the 10th cycle was carefully characterized as shown in Fig. 4. Compared to the SEM image of the pristine MOF-73 electrode (Fig. S5, ESI[†]), the surface of the cathode at 0.80 V was uniformly covered by irregular $\text{Zn}_4\text{SO}_4(\text{OH})_6 \cdot 5\text{H}_2\text{O}$ nanoplates generated at the full-discharge state and the remaining “ball-like” MnO_2 particles. Also, the EDS mapping (Fig. S7, ESI[†]) shows that the O and Mn elements are uniformly distributed in the “ball-like” particles and the O, Zn, and S are uniformly distributed in the nanoplates. The irreversible MnO_2 remained on the cathode surface after each cycle and could not be detected by XRD due to low crystallinity.⁴¹ When charged to 1.55–1.6 V, the “nanoflower-like” particles of zinc vernadite, $\text{Zn}_x\text{MnO}(\text{OH})_y$, appeared *via* the proton-diffusion reaction and the EDS mapping shows that these particles contain O, Zn and Mn elements but no S elements.^{42,43} At the states of 1.76–1.85 V, some newly formed MnO_2 particles were observed on the surface of $\text{Zn}_x\text{MnO}(\text{OH})_y$. Meanwhile, many ultra-thin nanosheets were generated. The main component elements of these nanosheets are O and Zn. When discharged to 0.8 V, the high activity of the $\text{Zn}_x\text{MnO}(\text{OH})_y$ particles and the emergence of $\text{Zn}_4\text{SO}_4(\text{OH})_6 \cdot 5\text{H}_2\text{O}$ can change the pH of the electrode surface, causing $\text{Zn}_x\text{MnO}(\text{OH})_2$ dissolution at the full discharge state. Specifically, the reversible mesophase $\text{Zn}_x\text{MnO}(\text{OH})_y$ particles began to appear at 1.55–1.60 V, indicating that the conversion and deposition of Mn^{2+} on the cathode do not result from the direct electrodeposition reaction (Mn^{2+} to MnO_2) but from the conversion of $\text{Zn}_x\text{MnO}(\text{OH})_y$ nanosheets.^{36,44,45}

According to the above discussion, the conversion Zn^{2+} storage mechanism of the MOF-73 cathode is illustrated in Fig. 5a and c. During the initial discharge process, $\text{Zn}_4\text{SO}_4(\text{OH})_6 \cdot 5\text{H}_2\text{O}$ forms on the surface of the electrode. In the latter cycle, the charge plateaus at ~ 1.55 V and ~ 1.60 V result from the Mn^{2+} interaction with $\text{Zn}_4\text{SO}_4(\text{OH})_6 \cdot 5\text{H}_2\text{O}$ nanoplates and turn into $\text{Zn}_x\text{MnO}(\text{OH})_y$ nanosheets, then part of $\text{Zn}_x\text{MnO}(\text{OH})_y$ transforms into ball-like MnO_2 nanoparticles. Subsequently, Zn^{2+} ions are extracted from MOF-73 (~ 1.76 V), and the last charge plateau emerges. In the following discharge process, the corresponding discharge plateau (~ 1.45 V) is generated with Zn^{2+} insertion into MOF-73. After that, the $\text{Zn}_x\text{MnO}(\text{OH})_y$ undergoes a proton solid-phase reaction but

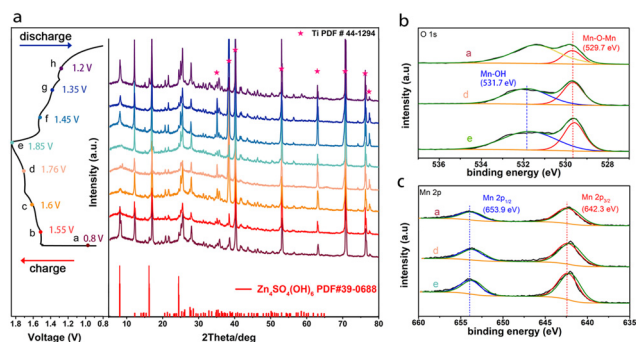


Fig. 3 (a) *Ex situ* XRD patterns of the MOF-73 cathode taken at different stages during a charge–discharge cycle. XPS patterns of the cathode (b) O1s and (c) Mn 2p at the voltages of a, d, e.

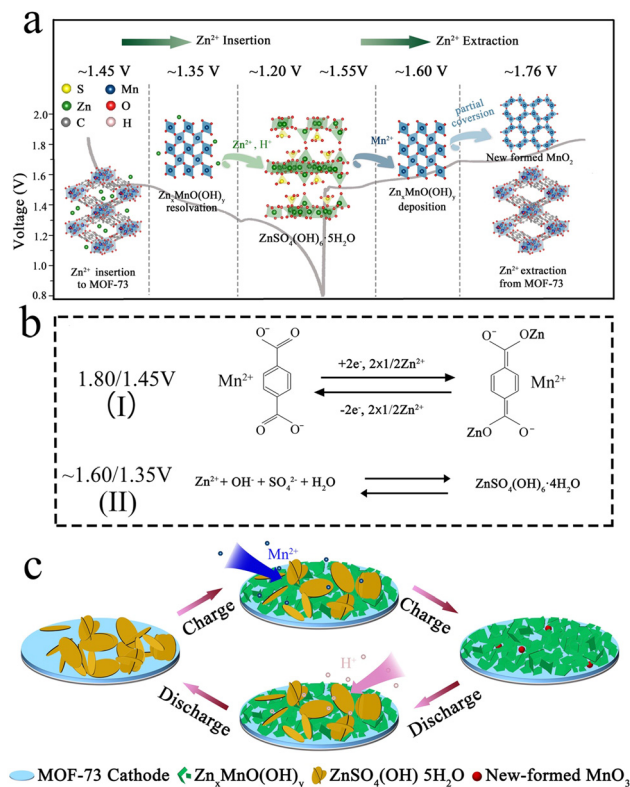


Fig. 5 (a and c) Schematic illustration of the Zn²⁺ storage mechanism and (b) chemical reaction equation of the Zn²⁺ insertion/extraction at different discharge/charge platforms of MOF-73 cathode.

Zn_xMnO(OH)_y nanosheets are gradually reduced by reacting with H⁺ (~1.35 V). With H⁺ consumption, Zn₄SO₄(OH)₆·5H₂O nanoplates are reformed on the cathode at the last discharge plateau (~1.20 V). The high activity of Zn_xMnO(OH)_y and the reformation of Zn₄SO₄(OH)₆·5H₂O change the pH of the electrode surface, causing Zn_xMnO(OH)_y dissolution at the full-discharge state. The chemical reaction equations to illustrate the above Zn²⁺ storage mechanism are displayed in Fig. 5b. According to the electrochemical mechanism of this kind of MOF electrode material in LIBs and SIBs, the reaction of MOF-73 is a two-electron transfer reaction between its keto and enol form. The capacity contribution at 1.60/1.35 V comes from the sedimentation/resolution of manganese and Zn₄SO₄(OH)₆·4H₂O on the electrode surface. Every subsequent charge/discharge cycle is consistently in agreement with this reversible electrochemical conversion reaction.

4. Conclusions

Here, we report MOF-73 as a cathode material for AZIBs, which delivers a high capacity of 815 mA h g⁻¹ (0.84 mA h cm⁻² at 50 mA g⁻¹). It has been illustrated by various *ex situ* measurements that MOF-73 can accomplish a discharge voltage at 1.45 V and induce the deposition of manganese ions to form Zn₄SO₄(OH)₆ and Zn_xMnO(OH)_y, co-contributing to a high-specific capacity. This work provides new fundamental insight

into the zinc storage mechanism of MOFs and can help to guide future efforts to explore new MOFs as competitive cathodes for AZIBs.

Author contributions

Wenshan Gou contributed to methodology, formal analysis, investigation, writing – original draft, visualization of this manuscript. Hao Chen, Zhao Xu, Yifei Sun, Xuguang Han and Mengmeng Liu contributed to methodology, formal analysis, visualization, data curation, data curation, visualization, conceptualization, formal analysis of this manuscript. Yan Zhang contributed to resources, writing – review & editing, supervision, project administration, funding acquisition of this manuscript.

Conflicts of interest

The authors declare no conflict of interest.

Acknowledgements

This work was supported by discipline construction funds from Qingdao Municipal Science and Technology Commission and Qingdao University (DC1900013623).

Notes and references

- 1 S. Chu, Y. Cui and N. Liu, *Nat. Mater.*, 2017, **16**, 16–22.
- 2 T. Jiang, S. Y. Ma, J. B. Deng, T. Yuan, C. F. Lin and M. L. Liu, *Adv. Sci.*, 2021, 2105119.
- 3 Y. R. Ouyang, H. J. Cao, H. J. Wu, D. B. Wu, F. Q. Wang, X. J. Fan, W. Y. Yuan, M. X. He, L. Y. Zhang and C. M. Li, *Appl. Catal.*, 2020, **B 265**, 118606.
- 4 D. B. Wu, C. Wang, H. J. Wu, S. Wang, F. Q. Wang, Z. Chen, T. B. Zhao, Z. Y. Zhang, L. Y. Zhang and C. M. Li, *Carbon*, 2020, **163**, 137–144.
- 5 B. Yong, D. T. Ma, Y. Y. Wang, H. W. Mi, C. X. He and P. X. Zhang, *Adv. Energy Mater.*, 2020, **10**, 2002354.
- 6 D. Kundu, S. H. Vajargah, L. W. Wan, B. Adams, D. Prendergast and L. F. Nazar, *Energy Environ. Sci.*, 2018, **11**, 881–892.
- 7 X. H. Zeng, J. N. Hao, Z. J. Wang, J. F. Mao and Z. P. Guo, *Energy Storage Mater.*, 2019, **20**, 410–437.
- 8 L. Ma, M. A. Schroeder, T. P. Pollard, O. Borodin, M. C. S. Ding, R. M. Sun, L. S. Cao, J. Ho, D. R. Baker, C. S. Wang and K. Xu, *Energy Environ. Mater.*, 2020, **3**, 516–521.
- 9 Y. N. Gao, H. Y. Yang, Y. Bai and C. Wu, *J. Mater. Chem. A*, 2021, **9**, 11472–11500.
- 10 X. Y. Liu, J. Yi, K. Wu, Y. Jiang, Y. Y. Liu, B. Zhao, W. R. Li and J. Zhang, *Nanotechnology*, 2020, **31**, 122001.
- 11 H. G. Qin, L. L. Chen, L. M. Wang, X. Chen and Z. H. Yang, *Electrochim. Acta*, 2019, **306**, 307–316.
- 12 Z. L. Li, S. Ganapathy, Y. L. Xu, Z. Zhou, M. Sarilar and M. Wagemaker, *Adv. Energy Mater.*, 2019, **9**, 1900237.



- 13 P. He, M. Y. Yan, G. B. Zhang, R. M. Sun, L. N. Chen, Q. Y. An and L. Q. Mai, *Adv. Energy Mater.*, 2017, **7**, 1601920.
- 14 L. B. Dong, W. Yang, W. Yang, Y. Li, W. J. Wu and G. X. Wang, *J. Mater. Chem. A*, 2019, **7**, 13810–13832.
- 15 L. Y. Zhang, L. Chen, X. F. Zhou and Z. P. Liu, *Adv. Energy Mater.*, 2015, **5**, 1400930.
- 16 M. H. Alfaruqi, V. Mathew, J. Gim, S. Kim, J. Song, J. P. Baboo, S. H. Choi and J. Kim, *Chem. Mater.*, 2015, **27**, 3609–3620.
- 17 C. Guo, H. M. Liu, J. F. Li, Z. G. Hou, J. W. Liang, J. Zhou, Y. C. Zhu and Y. T. Qian, *Electrochim. Acta*, 2019, **304**, 370–377.
- 18 H. L. Pan, Y. Y. Shao, P. F. Yan, Y. W. Cheng, K. S. Han, Z. M. Nie, C. M. Wang, J. H. Yang, X. L. Li, P. Bhattacharya, K. T. Mueller and J. Liu, *Nat. Energy*, 2016, **1**, 16039.
- 19 N. Zhang, F. Y. Cheng, J. X. Liu, L. B. Wang, X. H. Long, X. S. Liu, F. J. Li and J. Chen, *Nat. Commun.*, 2017, **8**, 405.
- 20 M. Sun, D. S. Liu, Y. F. Wang, W. L. Liu, M. M. Ren, F. G. Kong, S. J. Wang, Y. Z. Guo and Y. M. Liu, *ChemElectrochem*, 2019, **6**, 2510–2516.
- 21 M. J. Shi, B. Wang, Y. Shen, J. T. Jiang, W. H. Zhu, Y. J. Su, M. Narayanasamy, S. Angaiah, C. Yan and Q. Peng, *Chem. Eng. J.*, 2020, **399**, 125627.
- 22 Y. Q. Fu, Q. L. Wei, G. X. Zhang, X. M. Wang, J. H. Zhang, Y. F. Hu, D. N. Wang, L. C. Zuin, T. Zhou, Y. C. Wu and S. H. Sun, *Adv. Energy Mater.*, 2018, **8**, 1801445.
- 23 L. Guo, K. M. Wan, B. Liu, Y. Wang and G. Wei, *Nanotechnology*, 2021, **32**, 442001.
- 24 J. S. Meng, X. Liu, C. J. Niu, Q. Pang, J. T. Li, F. Liu, Z. Liu and L. Q. Mai, *Chem. Soc. Rev.*, 2020, **49**, 3142–3186.
- 25 C. Ye, Y. Jiao, D. L. Chao, T. Ling, J. Q. Shan, B. W. Zhang, Q. F. Gu, K. Davey, H. H. Wang and S. Z. Qiao, *Adv. Mater.*, 2020, **32**, 1907557.
- 26 C. Ye, J. Q. Shan, D. L. Chao, P. Liang, Y. Jiao, J. N. Hao, Q. F. Gu, K. Davey, H. H. Wang and S. Z. Qiao, *J. Am. Chem. Soc.*, 2021, **143**, 16902–16907.
- 27 H. Tan, Y. Zhou, S.-Z. Qiao and H. J. Fan, *Mater. Today*, 2021, **48**, 270–284.
- 28 W. S. Gou, T. Jiang, Q. Fan and Y. Zhang, *Chin. Chem. Lett.*, 2022, <https://www.elsevier.com/journals/chinese-chemical-letters/1001-8417>.
- 29 H. Chen, C. Dai, F. Xiao, Q. Yang, S. Cai, M. Xu, H. J. Fan and S. J. Bao, *Adv. Mater.*, 2022, **34**, e2109092.
- 30 M. Q. Wang, C. Ye, S. J. Bao, Y. Zhang, Y. N. Yu and M. W. Xu, *Analyst*, 2016, **141**, 1279–1285.
- 31 N. L. Rosi, J. Kim, M. Eddaoudi, B. Chen, M. O'Keeffe and O. M. Yaghi, *J. Am. Chem. Soc.*, 2005, **127**, 1504–1518.
- 32 L. Wang, C. Mou, Y. Sun, W. Liu, Q. Deng and J. Li, *Electrochim. Acta*, 2015, **173**, 235–241.
- 33 W. H. Zhang, A. Nefedov, M. Naboka, L. Cao and C. Woll, *Phys. Chem. Chem. Phys.*, 2012, **14**, 10125–10131.
- 34 Y. Zhang, H. N. Guo, W. Q. Li, Y. K. Huang, Z. T. Zhang, G. S. Liu and Y. J. Wang, *ChemSusChem*, 2019, **12**, 4160–4164.
- 35 L. E. Blanc, D. Kundu and L. F. Nazar, *Joule*, 2020, **4**, 771–799.
- 36 H. Chen, S. Cai, Y. Wu, W. Wang, M. Xu and S. J. Bao, *Mater. Today Energy*, 2021, **20**, 100646.
- 37 H. Chen, H. Kuang, F. Liu, Y. Wu, S. Cai, M. Xu and S. J. Bao, *J. Colloid Interface Sci.*, 2021, **600**, 83–89.
- 38 X. F. Shen, X. N. Wang, Y. R. Zhou, Y. H. Shi, L. M. Zhao, H. H. Jin, J. T. Di and Q. W. Li, *Adv. Funct. Mater.*, 2021, **31**, 2101579.
- 39 W. Chen, G. D. Li, A. Pei, Y. Z. Li, L. Liao, H. X. Wang, J. Y. Wan, Z. Liang, G. X. Chen, H. Zhang, J. Y. Wang and Y. Cui, *Nat. Energy*, 2018, **3**, 428–435.
- 40 Z. P. Feng, G. R. Li, J. H. Zhong, Z. L. Wang, Y. N. Ou and Y. X. Tong, *Electrochem. Commun.*, 2009, **11**, 706–710.
- 41 A. Monshi, M. R. Foroughi and M. R. Monshi, *World J. Nano Sci. Eng.*, 2012, **7**, 154–160.
- 42 S. Bodei, A. Manceau, N. Geoffroy, A. Baronnet and M. Buatier, *Cosmochim. Acta*, 2007, **71**, 5698–5716.
- 43 S. Grangeon, F. Warmont, C. Tournassat, B. Lanson, M. Lanson, E. Elkaim and F. Claret, *Eur. J. Mineral.*, 2017, **29**, 767–776.
- 44 Y. F. Huang, J. Mou, W. B. Liu, X. L. Wang, L. B. Dong, F. Y. Kang and C. J. Xu, *Nano-Micro Lett.*, 2019, **11**, 4949.
- 45 T. S. Zhang, Y. Tang, G. Z. Fang, C. Y. Zhang, H. L. Zhang, X. Guo, X. X. Cao, J. Zhou, A. Q. Pan and S. Q. Liang, *Adv. Funct. Mater.*, 2020, **30**, 2002711.

